A physics-constraint neural network for CO$_2$ storage in deep saline aquifers during injection and post-injection periods

Zhao, Mengjie; Wang, Yuhang; Gerritsma, Marc; Hajibeygi, Hadi

Citation (APA)
Zhao, M., Wang, Y., Gerritsma, M., & Hajibeygi, H. (2024). A physics-constraint neural network for CO$_2$ storage in deep saline aquifers during injection and post-injection periods. *Advances in Water Resources*, *193*, Article 104837. https://doi.org/10.1016/j.advwatres.2024.104837
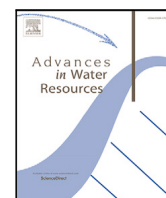
Important note
To cite this publication, please use the final published version (if applicable).
Please check the document version above.

A physics-constraint neural network for CO_2 storage in deep saline aquifers during injection and post-injection periods

Mengjie Zhao [a],[*], Yuhang Wang [b], Marc Gerritsma [a], Hadi Hajibeygi [c]

[a] *Faculty of Aerospace Engineering, Department of Flow Physics and Technology, Delft University of Technology, Kluyverweg 2, 2629 HS, Delft, The Netherlands*
[b] *School of Environmental Studies, China University of Geosciences, Wuhan 430078, China*
[c] *Faculty of Civil Engineering and Geosciences, Department of Geoscience and Engineering, Delft University of Technology, Stevinweg 1, 2628CV, Delft, The Netherlands*

ARTICLE INFO

ABSTRACT

CO_2 capture and storage is a viable solution in the effort to mitigate global climate change. Deep saline aquifers, in particular, have emerged as promising storage options, owing to their vast capacity and widespread distribution. However, the task of proficiently monitoring and simulating CO_2 behavior within these formations poses significant challenges. To address this, we introduce the physics-constraint neural network for CO_2 storage (CO_2PCNet), a model specifically designed for simulating and monitoring CO_2 storage in deep saline aquifers during injection and post-injection periods. Recognizing the significant challenges in accurately modeling the distribution and movement of CO_2 under varying permeability conditions, the CO_2PCNet integrates the principles of physics with the robustness of deep learning, serving as a powerful surrogate model. The architecture of CO_2PCNet starts with an encoder that adeptly processes spatial features from overall mole fraction (z_{CO_2}) and pressure fields (P_l), capturing the complex dynamics of a CO_2 trajectory. By incorporating permeability information through a conditioning step, the network ensures a faithful representation of the influences on CO_2 behavior in subsurface conditions. A ConvLSTM module subsequently discerns temporal evolutions, reflecting the real-world progression of CO_2 plumes within the reservoir. Lastly, the decoder precisely reconstructs the predictive spatial profile of CO_2 distribution. CO_2PCNet, with its integration of convolutional layers, recurrent mechanisms, and physics-informed constraints, offers a refined approach to CO_2 storage simulation. This model offers the potential of utilizing advanced computational methods in advancing CCS practices.

1. Introduction

The technology of carbon capture and storage (CCS) offers a promising solution to mitigate greenhouse gas emissions into the atmosphere (Selma et al., 2014; Orr Jr., 2018; Krevor et al., 2023). In CCS, the supercritical CO_2 is directly injected into geological formations, such as the depleted oil and gas reservoirs and deep saline aquifers, to achieve permanent sequestration (Zoback and Gorelick, 2012). The migration of the CO_2 plume within these subsurface systems is a complex interplay of viscous, gravitational, and capillary forces (Wang et al., 2024). Accurately predicting this migration and understanding the geomechanical responses are crucial for effective CCS project design, risk assessment (Pawar et al., 2015) and site characterization (Miocic et al., 2016). Nevertheless, the inherent interplay of different forces and heterogeneous geological structures complicate the long-term behavior and migration trajectory of CO_2 plumes. Numerical simulations, using high-fidelity models, are the primary method for predicting this multi-phase multi-component flow in porous media (Celia et al., 2015). Despite their accuracy, these simulations are computationally intensive and time-consuming due to the non-linear, multi-scale and multi-physics nature of the migration dynamics (Cusini et al., 2018; Xu et al., 2023). Moreover, the intrinsic uncertainties of rock-fluid properties add further computational burden, often requiring numerous forward simulation runs (Liu and Grana, 2020; Zhao et al., 2020).

Considering these computational and predictive challenges, there has been an increasing interest in the development of efficient surrogate models which present a balanced alternative for CCS projects and especially valuable in applications such as data assimilation and uncertainty quantification where conducting a prohibitive number of high-fidelity simulation runs becomes infeasible (Sun, 2020; Tang et al., 2022; Omosebi et al., 2022; Ju et al., 2023). Notably, deep-learning

---

(DL) surrogate models have demonstrated their potential in the field of computer vision (CV) (Ronneberger et al., 2022). A primary strength of DL is its robust capabilities for handling high-dimensional problems, enabling more efficient and accurate solutions. These DL models utilize statistical modeling to approximate the inputs and outputs based algorithms to capture the underlying physics principles (LeCun et al., 2015; Jiang and Durlofsky, 2024; Feng et al., 2024).

Recent studies have focused on the development and application of data-driven DL-based surrogate models to forest the relationships between reservoir attributes in the broad context of the fluid flow and transport problems in porous media (Wang et al., 2021; Zhao et al., 2023). These models utilize high-fidelity simulation data to construct statistical representations. Under appropriate configuration and training, these surrogates have the potential to accurately approximate even the most complex functions (Goodfellow et al., 2016). Among these, the convolutional neural network (CNN) has emerged as a particularly potent tool for image processing. Its strength lies in the ability to efficiently recognize spatial features and optimize the number of free parameters, thanks to the shared-weight architecture of its convolutional layers (Krizhevsky et al., 2012). Zhu and Zabaras (2018) first proposed a full CNN-based approach to estimate single-phase steady-state flows, aiming to predict pressure maps in heterogeneous environments with an encoder–decoder framework. Building on this, Mo et al. (2019b,a) applied a similar framework for forecasting the dynamic response of multi-phase flow in heterogeneous media. Meanwhile, Tang et al. (2020) introduced a Recurrent residual U-Net tailored for data assimilation in evolving subsurface flows. Moreover, certain network configurations have been adapted to address challenges associated with CO_2 storage. For instance, Wen et al. (2021a,b) modified the U-Net model to correlate permeability and injection parameters with CO_2 saturation maps and other attributes. Additionally, Yan et al. (2022) employed Fourier Neural Operators (FNO) to forecast the temporal and spatial evolution of CO_2 plumes during both the injection and subsequent post-injection periods.

While the recent advances in data-driven surrogate models for subsurface CO_2 storage, these models tend to extract insights predominantly from data, often overlooking the crucial underlying physical laws that govern these systems. Such an approach, while powerful, can sometimes yield predictions that, despite being statistically accurate, contradict established physical principles or intuitive expectations (Karniadakis et al., 2021). To address this limitation, a concept of physics-informed neural networks (PINNs) has recently received significant attention in the field of computational science (Raissi et al., 2019). PINNs are designed to solve nonlinear partial differential equations by integrating PDEs, initial conditions, and boundary conditions directly into the loss function of the neural network. This innovative approach allows PINNs to leverage initial condition data to solve PDEs, ensuring that the outcome is not only data-driven but also conforms to established physical laws. By integrating differential equations directly into the learning process, PINNs provide a powerful tool for modeling complex physical phenomena, particularly in scenarios where traditional data might be limited or sparse. Recent research has demonstrated the potential of combining PINNs with data-driven methods in various fields, from fluid dynamics (Zhu et al., 2019; Geneva and Zabaras, 2020; Ren et al., 2022) to solid mechanics (Goswami et al., 2022), thus demonstrating their ability to capture complex, multi-scale, and multi-physics phenomena.

In the context of CCS, where understanding the complex dynamics of CO_2 flow and transport in subsurface environments is important, PINNs offer a promising direction to enhance predictive modeling, and help to make predictions that are not just based on data, but also follow the basic rules of physics. Having introduced related work in CCS, we introduce CO_2PCNet — a novel surrogate model framework specifically designed for CO_2 storage. This framework adeptly merges the principles of PINNs with traditional data-driven methodologies, creating a synergistic model that excels in predicting the full-cycle

injection and migration scenarios. The core of CO_2PCNet is built around an encoder–decoder ConvLSTM, adept at capturing spatial features and their temporal evolution. The integration of physical PDEs as part of the loss function ensures that predictions are not only based on data but are also in line with physical laws. This approach makes the predictions of CO_2PCNet reliable and accurate, making it a powerful tool for CO_2 storage modeling.

The rest sections of the paper are organized as follows. Section 2 sets up the problem statement of CO_2 storage. In Section 3, we elaborate the CO_2PCNet's foundational principles and architecture designs. Section 4 presents the extensive numerical experiments and compares the performance between our networks and baseline methods. Section 5 discusses and concludes the observations as well as the outlook on future study.

2. Problem statement

2.1. Governing equations

For the problem of CO_2 and brine flow in multi-component multiphase systems, the foundational governing mass conservation equation is given by Wang et al. (2022):

$$\frac{\partial}{\partial t}(\phi \sum_{\alpha=1}^{n_{ph}} x_{c,\alpha} \rho_\alpha S_\alpha) + \nabla \cdot (\sum_{\alpha=1}^{n_{ph}} x_{c,\alpha} \rho_\alpha \boldsymbol{u}_\alpha) - \sum_\alpha x_{c,\alpha} q_\alpha = 0, \quad (2.1)$$

where ϕ denotes the porosity of the rock, and t indicates time. The variables α and c stand for the phases and components, respectively. Specifically, 'l' signifies the liquid phase and 'g' the gas phase, while CO_2 and brine are the components under consideration. The notation $x_{c,\alpha}$ describes the molar fraction of component c in phase α. The parameters S_α, ρ_α and q_α refer to the saturation, density, and source or sink terms of their respective phase α. Furthermore, $\boldsymbol{u}_\alpha$ is the Darcy velocity, as formulated in Darcy's Law, *i.e.*,

$$\boldsymbol{u}_\alpha = -\frac{kk_{r\alpha}}{\mu_\alpha}(\nabla P_\alpha - \rho_\alpha g \nabla h). \quad (2.2)$$

Here, k is the absolute permeability of rock, while $k_{r\alpha}$ and μ_α are the relative permeability and viscosity for phase α, respectively. The term g represents the gravitational acceleration, and h refers to the depth relative to a fixed reference point. P_α is the pressure of phase α and the capillary pressure P_c captures the interrelationship between different phases:

$$P_g - P_l = P_c(S_g), \quad (2.3)$$

where, P_g and P_l represent the pressures associated with the gas and liquid phases, respectively. In addition, it is assumed that the phases fill all pore spaces and the CO_2 and brine compositions also fill up the entire mixture, *i.e.*,

$$S_g + S_l = 1 \quad (2.4)$$

and

$$\sum_{c=1}^{n_c} x_{c,\alpha} = 1, \qquad \alpha = 1, \dots, n_{ph}. \quad (2.5)$$

2.2. Overall-compositional formulation

In this work, we adopt the overall composition variable set to solve the nonlinear equations of a two-component, two-phase system. The phase pressure and overall molar fraction are used as primary variables (Voskov and Tchelepi, 2012; Lyu et al., 2021). The overall mole fraction for component c, represented as z_c, is defined as

$$z_c = \sum_{\alpha=1}^{n_{ph}} \nu_\alpha x_{c,\alpha}, \qquad \forall c \in 1, \dots, n_c. \quad (2.6)$$

Here, ν_α represents the mole fraction of phase α, which can be described as a function of saturation, given by $\nu_\alpha = S_\alpha \rho_\alpha / \sum_{\alpha=1}^{n_{ph}} S_\alpha \rho_\alpha$. Utilizing

this defined overall molar composition, the mass conservation equation for each component can be reformulated as

$$\frac{\partial}{\partial t}(\phi \rho_T z_c) + \nabla \cdot (\sum_{\alpha=1}^{n_{ph}} x_{c,\alpha} \rho_\alpha \boldsymbol{u}_\alpha) = \sum_{\alpha=1}^{n_{ph}} x_{c,\alpha} q_\alpha, \qquad (2.7)$$

where $\rho_T = \sum_{\alpha=1}^{n_{ph}} S_\alpha \rho_\alpha$ represents the total density. Subsequently, the liquid phase pressure (P_l) and the CO_2 mole fraction, z_{CO_2}, are served as primary variables for the system. The numerical simulation of the above problem is conducted by a state-of-the-art fully physics numerical simulator DARSim. DARSim employs the finite difference system with fully implicit scheme (Zhang et al., 2023a).

2.3. Physical models

Given the significant influence of capillary pressure and the dissolution capability of CO_2 in brine, the mechanisms by which CO_2 can be retained in saline aquifers have been outlined by Metz et al. (2005). They are as follows: (a) Structural and stratigraphic trapping, (b) residual trapping, (c) dissolution trapping, and (d) mineral trapping. However, due to the slow nature of the reaction, mineral trapping is not considered in this study. Besides, we assume that CO_2 from the gas phase can dissolve in the liquid phase, but dissolution of brine in the gas phase is neglected (*i.e.* the gas phase contains only one component).

2.3.1. Dissolution

The solubility of CO_2 in brine is influenced by pressure, temperature and water salinity. For an isothermal system with a constant salinity, the CO_2-brine solution ratio, R_s, quantifies the amount of CO_2 that can be dissolved per unit volume of brine. Importantly, within each simulation cell, the potential quantity of dissolved CO_2 is constrained by the existing amount of CO_2. This highlights the significance of discerning the number of active phases in the cell (Hajibeygi and Tchelepi, 2014).

If a cell is in a two-phase state, the dissolved CO_2 amount can be extracted from a predefined CO_2-brine solution ratio curve, which is calculated prior to simulation, as shown in Fig. 1 A. Conversely, in an undersaturated state where only the liquid phase is present, R_s is determined using the mole fractions of the CO_2 component, *i.e.*,

$$R_s = \frac{\rho_b^{STC} z_{CO_2}}{\rho_{CO_2}^{STC}(1 - z_{CO_2})}, \qquad (2.8)$$

where the subscript 'b' denotes brine, while the superscript 'STC' signifies properties measured at standard conditions.

2.3.2. Capillarity

Capillary pressure, which is defined as the pressure differential between the wetting (liquid) and non-wetting (gas) phases, plays a crucial role in CO_2 storage. The interactions of these phases and the transport behavior of the matrix are governed by the relative permeability and capillary pressure functions, which are fundamental for the residual trapping mechanism. For example, rocks with low permeability and finer pore radius tend to display elevated capillary pressures compared to their high-permeability counterparts containing similar fluids. Such characteristics often result in CO_2 accumulating beneath structural and stratigraphic barriers at high saturations, especially when buoyant forces fail to counteract the capillary pressure imposed by the caprock narrow pore throat. In many sedimentary contexts, CO_2 typically acts as the non-wetting phase, while brine serves as the wetting phase. This interaction prompts brine to infiltrate the diminishing boundary of the CO_2 plume after injection (Wang et al., 2022). Such capillary movements lead to the formation of discrete, immobile CO_2 bubbles and ganglia, representing the residual trapping process. The intricacies of this mechanism are shaped by the rock inherent pore structure and wettability. This study utilized capillary pressure patterns through the Leverett J-function (Ruprecht et al., 2014), as illustrated in Fig. 1B and Fig. 1C.

3. Methodology

In this section, we start by briefly introducing the components and strategy of the neural network. Following this, we elaborate on the concept of CO_2PCNet. Lastly, we investigate how to incorporate the governing equation constraints into CO_2PCNet.

3.1. ConvLSTM

The Convolutional Long Short-Term Memory (ConvLSTM) introduces a novel paradigm in neural networks, specifically designed for modeling evolving long-term dependencies (Shi et al., 2015). By integrating the spatial characteristics of CNNs and the temporal capabilities of Long Short-Term Memory (LSTM) networks (Hochreiter and Schmidhuber, 1997), ConvLSTM provides a robust solution for multi-dimensional sequential data.

While LSTMs capture time-based patterns, they are less adept with spatial data. The ConvLSTM addresses this by replacing traditional LSTM matrix operations with convolutional operations. This preserves spatial information, such as pixel arrangements, while handling temporal sequences. Fundamentally, ConvLSTM employs memory cells and a gated system to mitigate the vanishing gradient issue seen in standard Recurrent Neural Networks (RNNs). Instead of fully-connected layers used in LSTMs, ConvLSTM incorporates convolutional layers, enhancing its spatial data handling.

The ConvLSTM processes information through a combination of gates and cells. The illustration is presented in Fig. 2. Let an input tensor at time t, represented as $\mathbf{X}^t$. The corresponding hidden state and cell state at this time are $\mathbf{h}^t$ and $\mathbf{C}^t$, respectively. The forget gate $\mathbf{f}^t$, governed by a sigmoid activation function, determines which segments of the previous memory should be retained or discarded. The input gate $\mathbf{i}^t$ establishes the amount of new data that will be stored into the cell state, while the internal cell $\widetilde{\mathbf{C}}^t$, influenced by a hyperbolic tangent activation layer, represents the potential new cell state. This collaborates with the input gate to finalize the information flowing into the actual cell state. Lastly, the output gate $\mathbf{o}^t$ derives the subsequent hidden state based on the current cell state and input. Formally, the ConvLSTM operations can be captured by the following equations:

$$\begin{aligned}
\mathbf{f}^t &= \sigma(\mathbf{W}_f * [\mathbf{h}^{t-1}, \mathbf{X}^t] + \mathbf{b}_f), \\
\mathbf{i}^t &= \sigma(\mathbf{W}_i * [\mathbf{h}^{t-1}, \mathbf{X}^t] + \mathbf{b}_i), \\
\widetilde{\mathbf{C}}^t &= \tanh(\mathbf{W}_c * [\mathbf{h}^{t-1}, \mathbf{X}^t] + \mathbf{b}_c), \\
\mathbf{C}^t &= \mathbf{f}^t \odot \mathbf{C}^{t-1} + \mathbf{i}^t \odot \widetilde{\mathbf{C}}^t, \\
\mathbf{o}^t &= \sigma(\mathbf{W}_o * [\mathbf{h}^{t-1}, \mathbf{X}^t] + \mathbf{b}_o), \\
\mathbf{h}^t &= \mathbf{o}^t \odot \tanh(\mathbf{C}^t),
\end{aligned} \qquad (3.1)$$

3.2. Auto-regressive model for CCS

Understanding and forecasting the evolution of critical parameters, the overall mole fraction z_{CO_2} and the liquid phase pressure P_l, is important for optimizing storage strategies and ensuring the safety and sustainability of the reservoir in the context of CO_2 storage. Due to the inherent complexity and non-linear dynamics present in these physical processes, an auto-regressive (AR) model is employed in this work (Geneva and Zabaras, 2020). This model, utilizing past system states to predict future states, offers a robust methodology for providing consistent insights into their evolving states.

The model incorporates the temporal dependencies intrinsic to the CO_2 storage process, casting them into a predictive framework. Enhanced with neural network capabilities, the AR model predicts the subsequent state at time $t + 1$ using the state variables at time t. Given the initial state $\mathbf{Y}^0 = [z_{CO_2}^0, P_l^0]$ and the static reservoir variables $\mathbf{K} = [\mathbf{k}_1, \dots, \mathbf{k}_{n_k}]$, sequence of dynamic variables rollout is computed as:
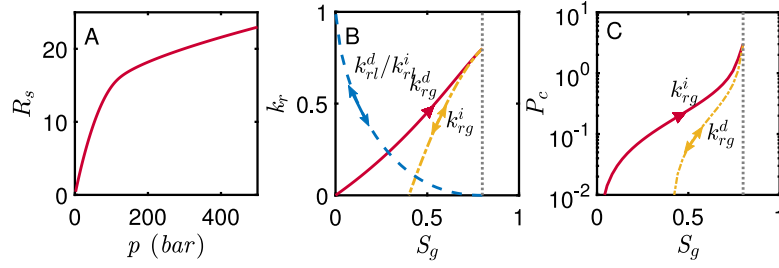
Fig. 1. Setup of physical models. (A) Predicted solubilities of CO_2 in brine at 60 °C. (B) Relative permeability curves: primary drainage and imbibition curves for both liquid and gas phases. Superscripts d and i represent drainage and imbibition, respectively. A single-headed arrow denotes an irreversible process along a given curve, while a double-headed arrow indicates reversibility. (C) Capillary pressure curves: primary drainage and imbibition curves.
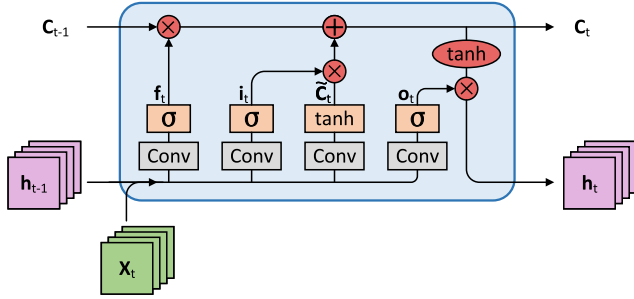

Fig. 2. Schematic Representation of a ConvLSTM Cell.

$[\hat{\mathbf{Y}}^1, \ldots, \hat{\mathbf{Y}}^{n_t}]$. Mathematically, the evolving states of the system can be represented as

$$\hat{\mathbf{Y}}^0 = \mathbf{Y}^0, \tag{3.2}$$

$$\hat{\mathbf{Y}}^{t+1} = \mathcal{F}(\hat{\mathbf{Y}}^t, \mathbf{K}, \theta), \qquad t \in 1, \ldots, n_t. \tag{3.3}$$

Here, $\hat{\mathbf{Y}}^{t+1}$ represents the predicted state of the system at the next time step $t + 1$, $\mathbf{K}$ is the static variables (*i.e* the permeability fields), and $\mathcal{F}$ denotes a neural network mapping with θ as its parameters. The formulation allows the neural network to determine the mapping function $\mathcal{F}$ between the static variables and dynamic state variables, facilitating the computation of the dynamic variables at new time steps.

In essence, this neural network operates as a time integrator, where the output of each sequence is fed into the next layer as input, thereby functioning fundamentally as an AR model.

3.3. Network architecture: CO₂PCNet

In order to develop robust and accurate modeling approaches for CO_2 storage dynamics, the CO_2PCNet architecture is formulated to learn the complex temporal and spatial dependencies intrinsic to CO_2 storage data sequences. This network consists of three principal components: (1) the encoder, (2) the ConvLSTM, and (3) the decoder, as illustrated in Fig. 3.

Initially, the encoder, which includes three convolutional layers, adeptly compresses the provided input into a low-dimensional latent space, thereby encapsulating the spatial features crucial for accurate predictive modeling (Krizhevsky et al., 2012). The Swish activation function is employed for the convolutional layers to introduce the non-linearity, fostering more complex representations (Ramachandran et al., 2017).

Following the encoding phase, the resultant spatial embeddings are channeled into the ConvLSTM layer. This layer, characterized by its recurrent neural network structure, is designed to simultaneously decode spatial patterns and their temporal evolution.

Subsequently, the ConvLSTM layer's outputs are transformed through an upsampling operation, effectively reconstructing the low-resolution latent embeddings into high-resolution predictive outputs

(Ronneberger et al., 2022). Specifically, this decoder phase is a combination of upsampling and an additional convolution layer, consisting of three stages to refine and project the latent space into detailed output predictions. Consequently, the dynamic variables $z_{CO_2}^{t+1}$, P_l^{t+1} at time instant $t+1$ are concatenated with the static variables, setting the stage for the inputs at the next time step, $t+2$. The detailed structures of the encoder and decoder blocks are depicted in Fig. 4.

Incorporating an auto-regressive strategy within CO_2PCNet, the network is designed to ensure that each sequential prediction ($t+1, t+2, \ldots$) is based on the information of preceding state. This approach effectively captures the evolving dynamics of the system over time, allowing the network to adaptively refine its predictions based on the continuously updated data. Consequently, this results in forecasts that are progressively informed and accurate, as the model processes more data.

CO_2PCNet employs a consistent architectural framework throughout all phases of CO_2 storage, from injection to post-injection. This approach ensures seamless transitions between simulation phases by using outputs from prior time steps as inputs for subsequent predictions, thus maintaining a coherent and continuous flow of data throughout the model's operation.

The model's capacity for iterative refinement, informed by its autoregressive framework, offers a robust alternative to traditional simulators for understanding CO_2 storage processes, particularly valuable for tasks such as uncertainty quantification and history matching. Moreover, the integration of an encoder–decoder ConvLSTM within this auto-regressive framework significantly enhances the functionality. This integration enables the efficient extraction and interpretation of spatial features while simultaneously monitoring their temporal development.

3.4. Loss function

Another critical aspect of CO_2PCNet's effectiveness lies in its ability to ensure that predicted CO_2 distributions conform closely to the fundamental physical laws governing subsurface flow processes. Our model incorporates these laws directly within its architecture and loss function to ensure that predictions not only match observational data but also align with physical principles. Therefore, we formulate a loss function that guarantees the outputs of the neural network remain faithful to the physical constraints inherent to the domain of interest.

The training strategy of CO_2PCNet leverages an autoregressive approach, which processes sequential data by using the prediction from a current time step as the input for the next, facilitating a dynamic modeling of temporal dependencies. This design is important for calculating the discretized PDE residuals of (Eq. (2.7)), which form an integral part of the physics-constraint term in our loss function. By embedding these calculations within the network, CO_2PCNet effectively captures the dynamic behavior of CO_2 plume evolution and pressure distribution across the geological formation.

The total loss function, denoted as $\mathcal{L}$, is composed of three primary elements: the data mismatch term $\mathcal{L}_{\text{Data}}$, the physics-constraint term
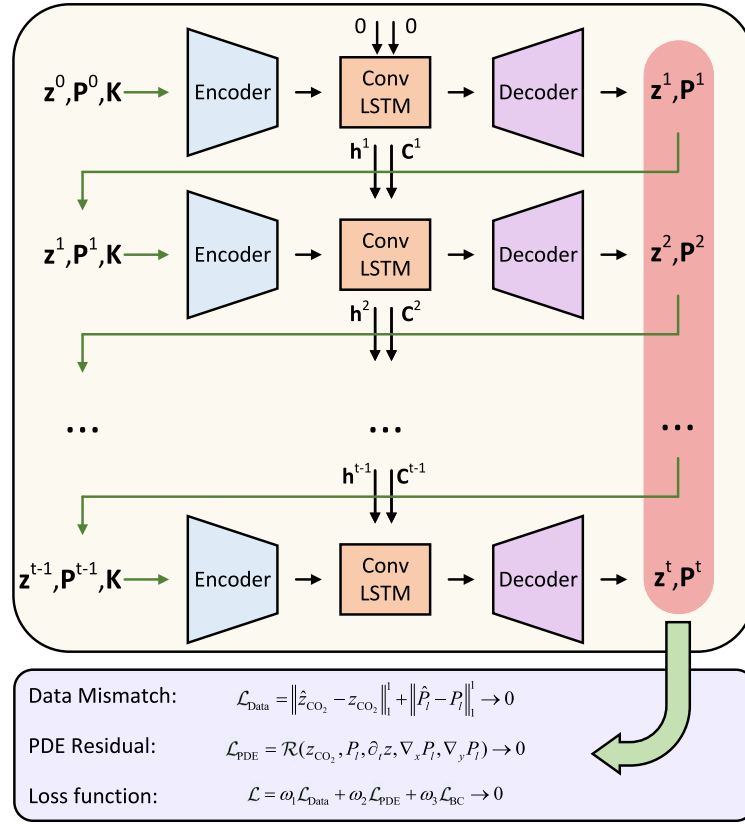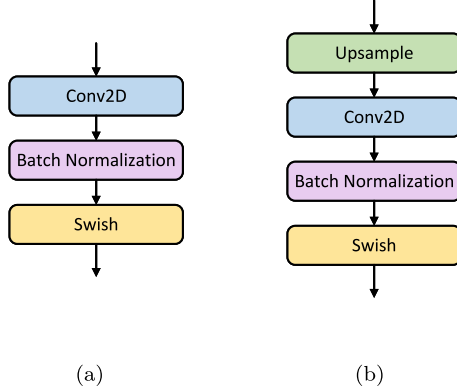
Fig. 3. The network architecture of CO₂PCNet.

Fig. 4. Illustrations of the Convolutional Block and Upsampling Convolutional Block: (a) Encoder. (b) Decoder.

$\mathcal{L}_{\text{PDE}}$, and the boundary condition term $\mathcal{L}_{\text{BC}}$. It is worth noting that, regarding the initial conditions, the state variables are known and thus, there is no specific term for initial conditions in our loss function.

The data mismatch term $\mathcal{L}_{\text{Data}}$ measures the difference between the network predictions and the actual observed data. For our model, we utilize the mean absolute error (MAE) of mole fraction and pressure fields, chosen due to its robustness. This metric is widely used as a loss function, *i.e.*,

$$\mathcal{L}_{\text{Data}} = \frac{1}{n_t n_s n_g} \sum_{t=1}^{n_t} \sum_{i=1}^{n_s} \sum_{j=1}^{n_g} (\|(\hat{z}_{\text{CO}_2})_{i,j}^t - (z_{\text{CO}_2})_{i,j}^t\|_1^1 + \|(\hat{P}_l)_{i,j}^t - (P_l)_{i,j}^t\|_1^1), \quad (3.4)$$

where, n_s is the number of samples, and $n_g = 32 \times 128 = 4096$ represents the number of grid blocks. The terms $(\hat{z}_{\text{CO}_2})_{i,j}^t$ and $(\hat{P}_l)_{i,j}^t$ correspond to the predicted mole fraction and pressure, respectively, for training

sample i, within grid block j, at time step t. $(z_{\text{CO}_2})_{i,j}^t$ and $(P_l)_{i,j}^t$ are the actual, or ground truth values of mole fraction and pressure. This loss term ensures the output of network is closely aligned with the observed data, maintaining the accuracy of the model in capturing CO₂ behavior. In our auto-regressive model, errors at each timestep are calculated and influence the total loss, leading to updates across the entire model. This setup ensures continuous improvement through backpropagation, where early errors adjust model parameters, enhancing predictions across the entire timeline. Thus, the model learns from discrepancies at any point in the sequence, refining its performance iteratively to boost overall accuracy throughout the learning process.

The physics-constraint term $\mathcal{L}_{\text{PDE}}$ plays an important role in ensuring that CO₂PCNet's predictions following the fundamental physical laws governing the subsurface fluid dynamics. This term is defined as the residuals of the PDEs for the two-component system involving CO₂ and brine, ensuring mass conservation are represented:

$$\mathcal{L}_{\text{PDE}} = \|\mathcal{R}(z_{\text{CO}_2}, P_l, \partial_t z, \nabla_x P_l, \nabla_y P_l)\|_1^1, \quad (3.5)$$

where, $R(\cdot)$ represents the residuals of the mass conservation equations as specified in Eq. (2.7), aiming for these residuals to approach zero to indicate physical consistency. It encapsulates the mass conservation laws that are critical for modeling flow in porous media.

Derivatives within the PDE constraints are enforced across the entire spatiotemporal domain of our model to ensure that the temporal dynamics and spatial distributions adhere to the physical behavior. This is achieved by discretizing the domain and applying differential equation constraints at each grid point. Specifically, spatial derivatives are computed using finite difference schemes, which are essential for local conservation laws. The discrete temporal derivatives are calculated between time steps, capturing the dynamics of CO₂ behavior over time. For instance, consider the derivative of liquid pressure (P_l) with respect to spatial coordinates, which can be approximated by:

$$\left(\frac{\partial P}{\partial x}\right)_{i+\frac{1}{2},j}^t = \frac{P_{i+1,j}^t - P_{i,j}^t}{1/2(\Delta x_i + \Delta x_{i+1})} \quad (3.6)$$
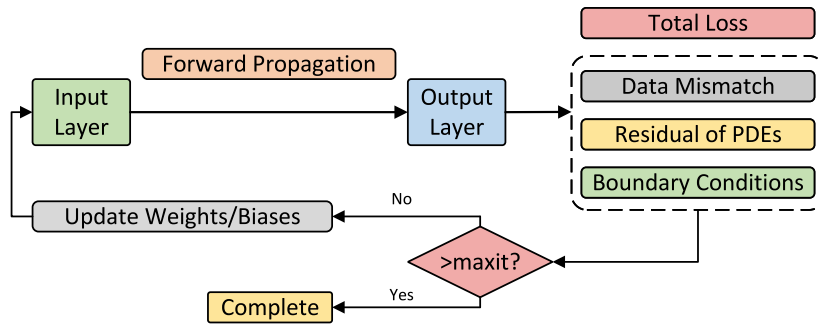
Fig. 5. Flowchart illustrating the physics enforcement mechanism in CO$_2$PCNet. The process ensures that each prediction adheres to established physical laws, thereby enhancing the reliability and accuracy of the model outputs.
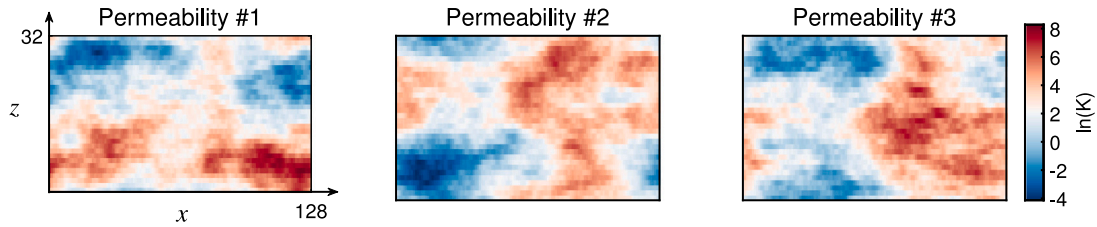

Fig. 6. Three cases of heterogeneous permeability realizations.

The boundary condition term, $\mathcal{L}_{BC}$, is formulated to both constrain and penalize deviations from the pre-defined boundary conditions, defined as:

$$\mathcal{L}_{BC} = \|\hat{u} - u_{BC}\|_1^1, \tag{3.7}$$

The total loss function is a weighted sum of these three terms, *i.e.*,

$$\mathcal{L} = \omega_1 \mathcal{L}_{Data} + \omega_2 \mathcal{L}_{PDE} + \omega_3 \mathcal{L}_{BC}. \tag{3.8}$$

where ω_1, ω_2 and ω_3 are hyperparameters that balance the influence of each term. The choice of these values is critical and is typically determined through experimentation to find the best model performance. In this work, equal weights are chosen for all terms, thus maintaining a balanced contribution from each aspect of the loss function to the overall learning process. Fig. 5 illustrates the step-by-step process of our physics enforcement algorithm.

4. Numerical experiments and results

In this section, we assess the performance of our method in CO$_2$ storage simulations. The evaluation includes: (1) testing CO$_2$PCNet's ability to forecast responses under different permeability fields; (2) comparing CO$_2$PCNet's solution accuracy and generalization ability with baseline algorithms.

4.1. Dataset generation

To facilitate the training and evaluation the CO$_2$PCNet in deep saline aquifers, a 2-D CCS simulation system is implemented. From the geological perspective, recognizing the important role of gravity in the CO$_2$ trapping process, a 2-D representation in the xz-plane is adopted, because gravity plays a significant role in the migration and trapping of CO$_2$ in saline aquifers. Aquifers are generally characterized by a longer longitudinal length compared to their cross-sectional width. Therefore, the dimensions of our simulation domain are set to 128 m × 32 m in the xz-direction and the grid is uniformly discretized into 1 m × 1 m cells. This setup effectively simulates the migration patterns of CO$_2$ within a 2-D vertical cross-section of an aquifer, providing a conceptual representation of its behavior in such geological contexts. It is worth noting that the architecture of CO$_2$PCNet is scalable and

can be adapted to larger, more realistic reservoir sizes as computational resources allow.

In order to mimic the geological formations for CO$_2$ storage, a total 1200 permeability realizations were generated using the Stanford Geostatistical Modeling Software (SGeMS), an open-source tool for geostatistical modeling (Remy et al., 2009). These permeability fields, which are log-normally distributed with a mean $\ln K$ of 2.5 and a standard deviation of 2, are depicted in Fig. 6, showing three example realizations. The heterogeneity in permeability is critical for quantifying the impact of uncertain reservoir properties. By incorporating a wide range of permeability scenarios, our simulation framework allows for a detailed analysis of CO$_2$ migration and trapping behaviors under varying geological permeability conditions.

For the simulation settings, the initial pressure is set at 2.5×10^7 Pa, with a constant temperature of 300 K. No flow boundary conditions are applied to all sides of the aquifer. CO$_2$ is injected at a consistent rate of 1×10^{-4} pore volumes per day along the entire left boundary, with a production well is placed along the entire right boundary (Nordbotten and Celia, 2006; Ide et al., 2007). The planned simulation duration is 2520 days, including a 600 days injection phase followed by a 1920 days post-injection phase. The total period is evenly divided into 21 intervals, with each lasting 120 days. The forward simulations are performed using DARSim, and Table 1 presents the physical parameters and configurations utilized in the DARSim numerical simulation. Our model, which addresses the complex dynamics of multi-component, multi-phase interactions in CO$_2$ storage in deep saline aquifers, adopts a conservative extrapolation period.

4.2. Baseline model setup

The baseline model is trained using neural architectures similar to those employed in our proposed CO$_2$PCNet to ensure a fair comparison. We mainly compare the solution snapshots between CO$_2$PCNet — our physics-constraint network and CO$_2$Net, which operates without the incorporation of physics constraints. This comparison aims to discern the impact and efficacy of integrating physical laws directly into the neural network's learning process.

For the setup of neural networks, the encoder of the network features three convolutional layers with channel sizes of 16, 32, and 128 units, using 3 × 3 kernels. The strides for these layers are set to 2,
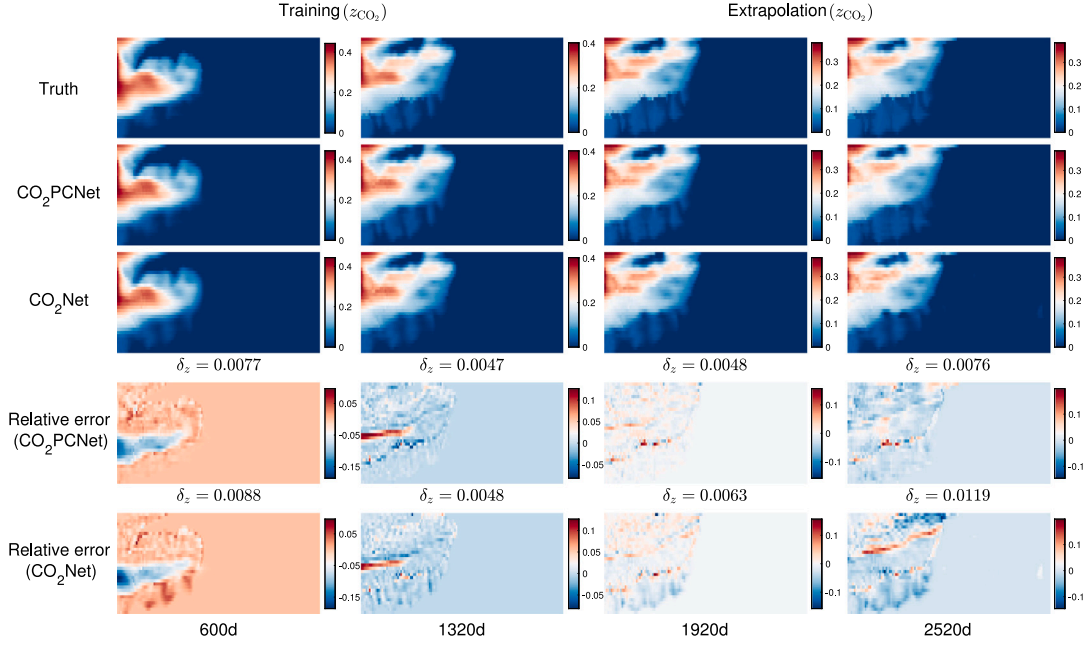
Fig. 7. Temporal evolution of z_{CO_2}. Numerical simulations (first row), CO_2PCNet predictions (second row), and CO_2Net predictions (third row) are compared at four time steps. Relative errors for CO_2PCNet (fourth row) and CO_2Net (fifth row) are depicted. The left two columns show results within the training period, while the right two columns represent extrapolations.

Table 1
Physical parameters and simulation setup for the darsim numerical simulation.

Parameter	Value	Unit
Aquifer length	128	m
Aquifer height	32	m
Porosity	0.2	–
CO_2 injection rate	1×10^{-4}	pore volumes per day
Initial pressure	2.5×10^7	Pa
Bottom hole pressure	2.5×10^7	Pa
Temperature (isothermal)	300	K
CO_2 density at STC	1.98	kg/m^3
Brine density at STC	1060	kg/m^3
Brine salinity	1×10^5	parts per million

1, and 2, respectively, facilitating effective data compression. Following the encoder, the network employs a ConvLSTM layer with 128 hidden units, designed to process temporal information using 3×3 kernels and a stride of 1. The decoder, tasked with reconstructing the output, mirrors this approach using similar kernels and strides for upsampling.

CO_2PCNet and CO_2Net are trained with data from the first 15 time steps, encompassing 1800 days. This training phase incorporates 1000 permeability scenarios. Subsequently, the forecasting capabilities of the network are evaluated based on its predictions for the next 6 time steps, representing an additional 720 days. During this evaluation phase, a uniform set of 200 permeability fields is employed, ensuring a consistent framework for forecasting. Notably, to standardize the data, min–max normalization is applied to the output values. The network model employs the adaptive moment estimation (Adam) optimizer for training, starting with an initial learning rate of 0.001 (Kingma and Ba, 2014). The number of training epochs used is 1000, and the minibatch size is 20. In our experiments, the training time for CO_2PCNet was around 8 h, while CO_2Net required approximately 6.5 h. This additional training duration for CO_2PCNet is primarily due to the integration of physical constraints into the learning process.

In the context of CO_2 storage in deep saline aquifers, two essential parameters - R_s and S_g, representing CO_2 solubility in liquid and gas phases, are calculated from the predicted mole fraction z_{CO_2} and

pressure P_l. These predictions also are compared to the ground truth to assess the model's accuracy in simulating CO_2 distribution and behavior in these complex geological formations.

4.3. Evaluation metrics

Quantifying the relative error in CO_2PCNet predictions for z_{CO_2} and P_l is essential for assessing the model's accuracy. The relative error for the mole fraction at a given time step t, denoted δ_z^t, for the entire set of $n_s = 200$ test samples, is calculated as

$$\delta_z^t = \frac{1}{n_s n_g} \sum_{i=1}^{n_s} \sum_{j=1}^{n_g} \frac{|(\hat{z}_{CO_2})_{i,j}^t - (z_{CO_2})_{i,j}^t|}{(z_{CO_2})_{i,\max}^t - (z_{CO_2})_{i,\min}^t}, \tag{4.1}$$

where, $(\hat{z}_{CO_2})_{i,j}^t$ and $(z_{CO_2})_{i,\max}^t$ represent the predicted and actual mole fraction values for test sample i, in grid block j, at time step t, respectively. The normalization factor, $(z_{CO_2})_{i,\max}^t - (z_{CO_2})_{i,\min}^t$, is the difference between the maximum and minimum grid-block mole fraction values for sample i at time step t. The evaluation of pressure predictions follows a similar methodology, *i.e.*,

$$\delta_P^t = \frac{1}{n_s n_g} \sum_{i=1}^{n_s} \sum_{j=1}^{n_g} \frac{|(\hat{P}_l)_{i,j}^t - (P_l)_{i,j}^t|}{(P_l)_{i,\max}^t - (P_l)_{i,\min}^t}. \tag{4.2}$$

To obtain a comprehensive view of the model's performance over time, the overall relative mole fraction and pressure errors across n_t time steps, denoted δ_z and δ_z respectively, are the calculated as

$$\delta_z = \frac{1}{n_t} \sum_{t=1}^{n_t} \delta_z^t \tag{4.3}$$

and

$$\delta_P = \frac{1}{n_t} \sum_{t=1}^{n_t} \delta_P^t. \tag{4.4}$$

These metrics are employed to assess the performance of the proposed network model under various scenarios, offering insights into its predictive capabilities and accuracy.
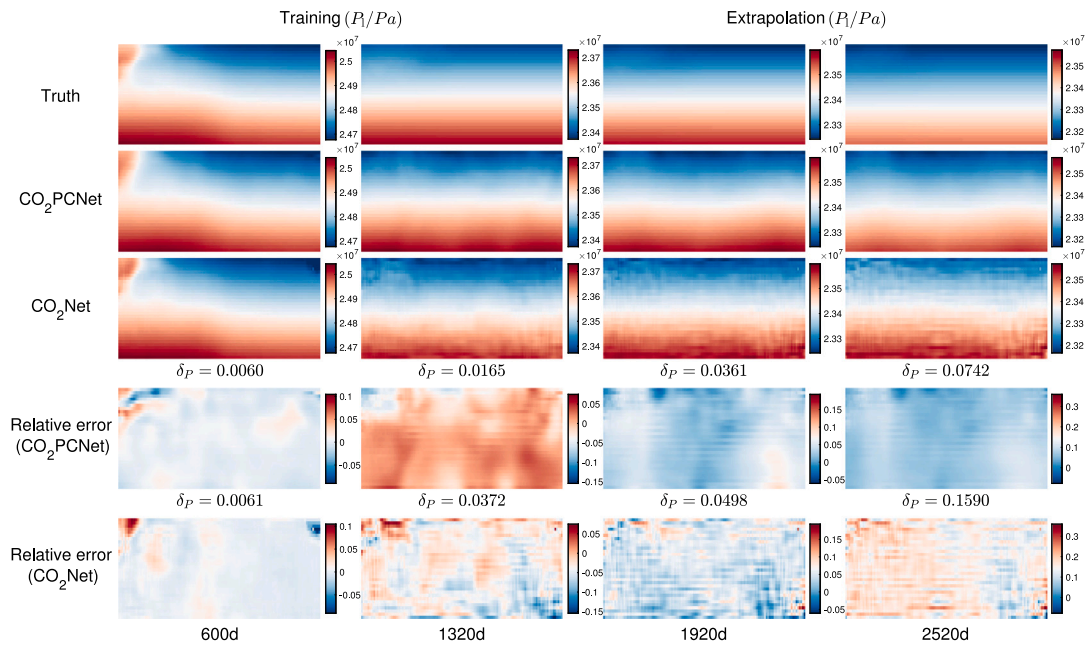
Fig. 8. Temporal evolution of liquid pressure P_l in pascals (Pa). Numerical simulations (first row), CO_2PCNet predictions (second row), and CO_2Net predictions (third row) are compared at four time steps. Relative errors for CO_2PCNet (fourth row) and CO_2Net (fifth row) are depicted. The left two columns show results within the training period, while the right two columns represent extrapolations.
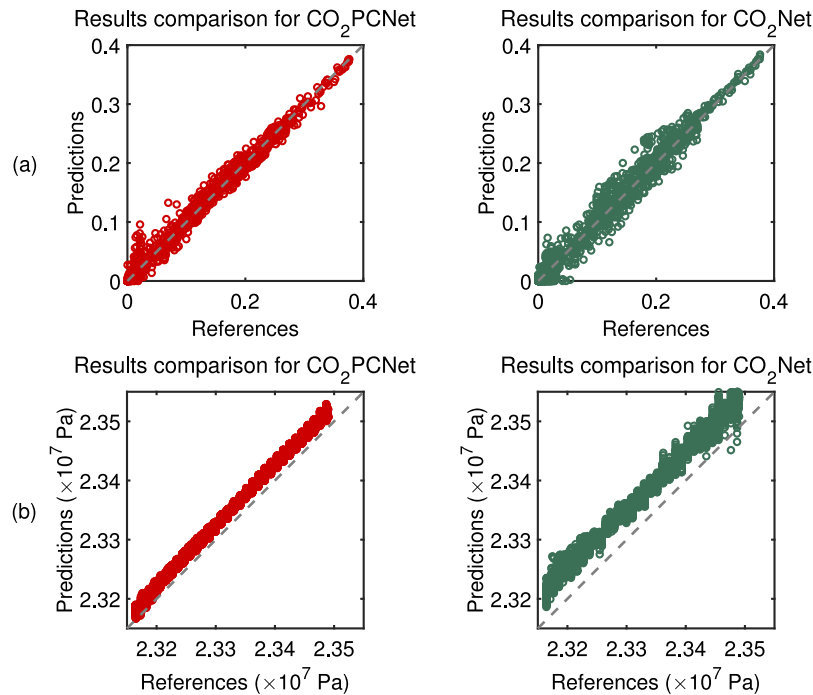

Fig. 9. Scatter plots of Predictions vs. Reference Values at 2520 days: (a) z_{CO_2} and (b) P_l. Predictions by CO_2PCNet are on the left, while CO_2Net's are on the right, each plotted against the high-fidelity simulation reference. Each point represents a predicted value plotted against its corresponding reference value, with the line of perfect agreement shown as a dashed line for reference.

4.4. Forecasting future responses

In this case, we first evaluate the performance of CO_2PCNet and CO_2Net in forecasting CO_2 behavior beyond the training period. Figs. 7 and 8 present a comparison between the CO_2PCNet's predictions of the mole fraction (z_{CO_2}) and the liquid pressure (P_l) for Permeability #1 (shown in Fig. 6) with the high-fidelity simulation results and baseline algorithm CO_2Net at four snapshots (t = 600, 1320 days in the training period, t = 1920, 2520 days beyond the training period). Below each

prediction, the mean relative absolute error δ_z and δ_P are indicated. These snapshots capture the transition from observed dataset to the predictive phase, where the generalization of the model's capacity is tested against the complexities of the system evolution.

Upon CO_2 injection into the saline aquifer, the CO_2 starts to displace the existing brine within the porous media. The CO_2 tends to rise due to its lower density relative to the brine. This migration is governed by a complex interplay of gravity, capillary pressure, and the permeability of the rock. Simultaneously, as CO_2 dissolves in the brine, it increases
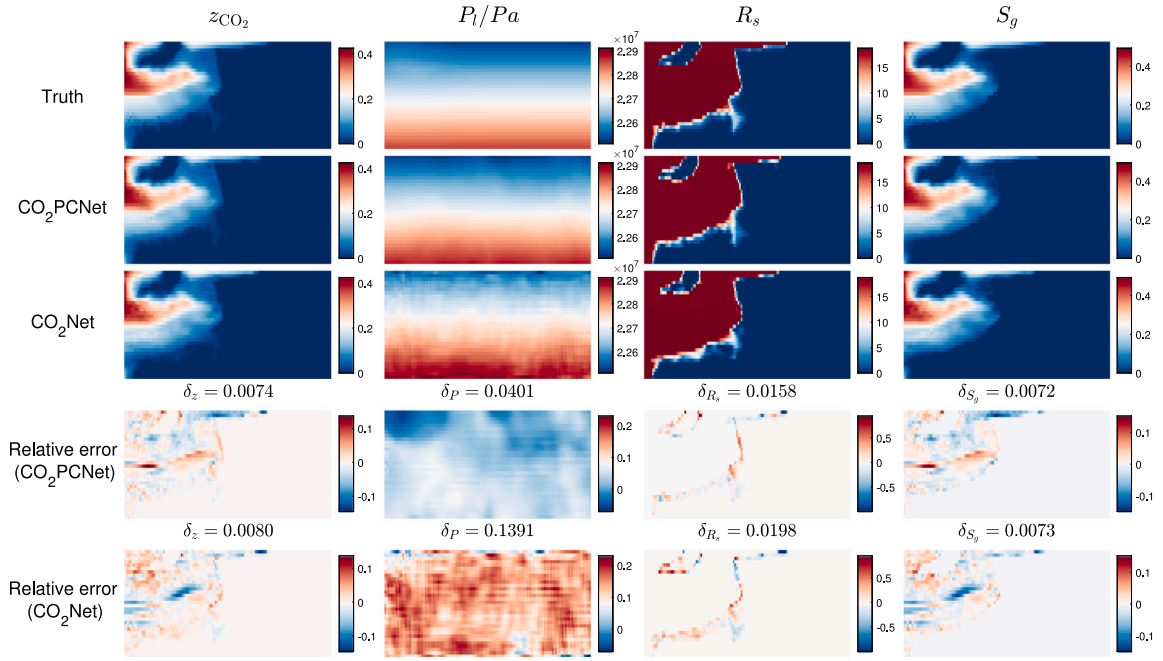
Fig. 10. Test case 1: Predictions of z_{CO_2}, liquid pressure P_l in pascals (Pa), R_s and S_g at 2520 days. The top row represents the numerical simulation 'Truth', followed by CO_2PCNet and CO_2Net predictions. The bottom two rows quantify the relative errors for CO_2PCNet and CO_2Net, respectively.
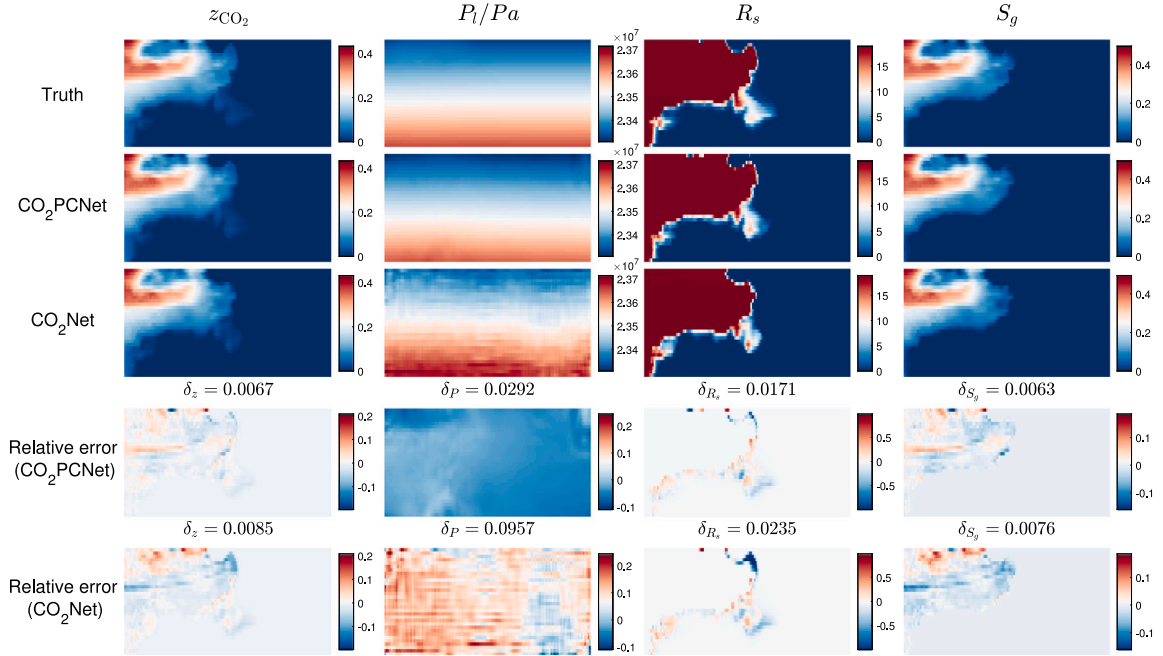
Fig. 11. Test case 2: Predictions of z_{CO_2}, liquid pressure P_l in pascals (Pa), R_s and S_g at 2520 days. The top row represents the numerical simulation 'Truth', followed by CO_2PCNet and CO_2Net predictions. The bottom two rows quantify the relative errors for CO_2PCNet and CO_2Net, respectively.

the density of brine, causing it to descend and thereby promoting further dispersion of CO_2. The pressure distribution observed during the injection phase is typically higher near the injection site, gradually decreasing outward as CO_2 displaces the brine and the system approaches pressure equilibrium. Following injection, the pressure profile demonstrates a gradual decrease to reach a new equilibrium.

Both models exhibit close alignment with the high-fidelity simulations during the training phase, demonstrating their capability to accurately learn and replicate the dynamics of CO_2 distribution. However, as the model progresses into the extrapolation phase, a distinct divergence becomes apparent. CO_2PCNet's predictions preserve a more

consistent accuracy, reflected in the tighter error distributions as time advances. In contrast, the errors from CO_2Net, particularly in predicting P_l fields, appear to grow, which suggests that the integration of physics constraints in CO_2PCNet plays a significant role in ensuring the consistency and accuracy over longer prediction intervals. Although relative error margins naturally widen as the model projects further into the future, CO_2PCNet's outputs remain reasonably accurate, remaining within acceptable error. Additionally, it is worth noting that the relative errors in pressure predictions are distributed across the entire domain due to the elliptic nature of the pressure variable.
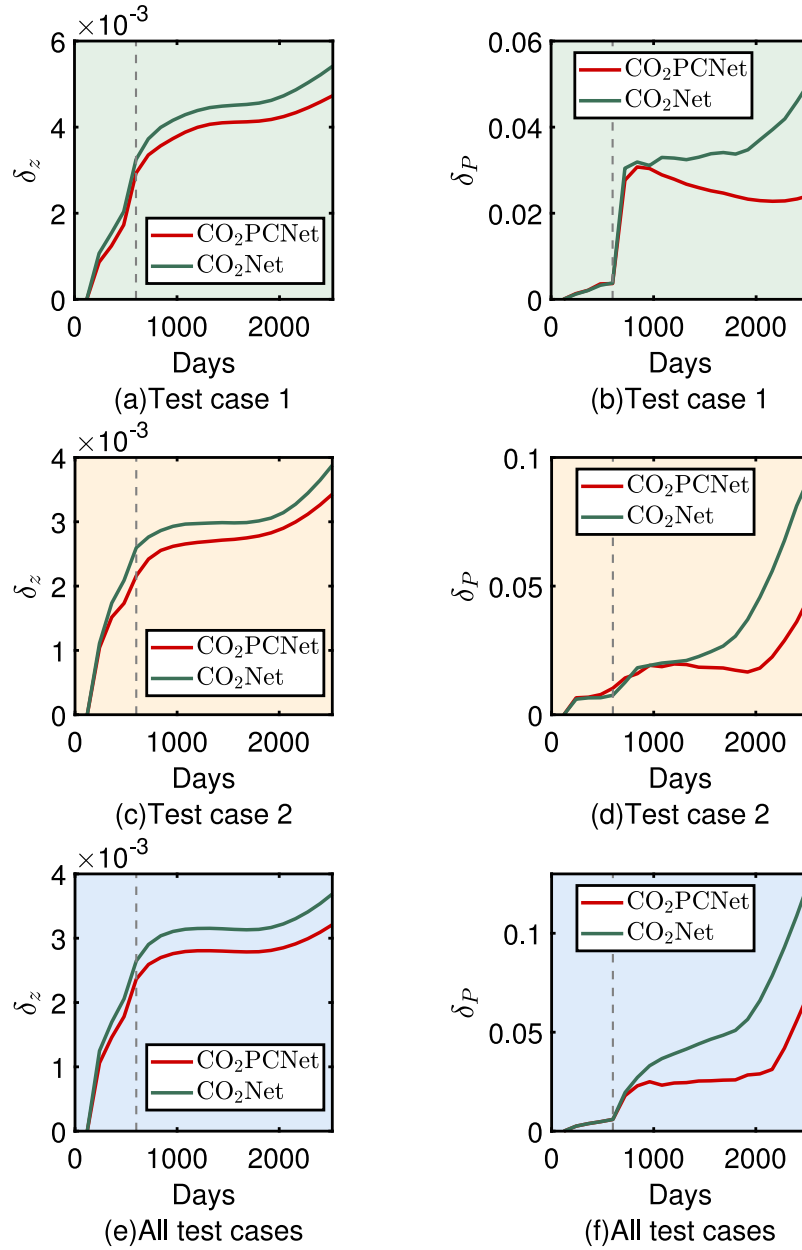
Fig. 12. Mean relative error trends for CO_2PCNet and CO_2Net over a period of 2520 days across two test cases and all 200 test cases. The vertical dashed lines represent the stop of CO_2 injection.

To further compare the results at the final time step, Fig. 9 provides an insightful comparison of the predictions from CO_2PCNet and CO_2Net against the reference simulations. CO_2PCNet's predictions for both z_{CO_2} and P_l closely align with the reference values, forming a dense cluster around the line of perfect agreement. This indicates high predictive accuracy and a strong correlation between the predicted and actual values. CO_2Net, while still maintaining a reasonable correlation for z_{CO_2}, predictions for P_l show a more significant deviation from the reference line, which suggests a less precise match to the reference data.

4.5. Forecasting future responses with new permeability fields

In this subsection, the CO_2PCNet model is further tested by predicting CO_2 behavior during both active injection and post-injection phases in scenarios with new permeability fields not encountered during training. This generalization capability is critically important for the applications of neural network models as surrogate models in the context of uncertainty quantification, where the model is required to make accurate predictions for various permeability maps.

Figs. 10 and 11 compare the predictions from CO_2PCNet with those from CO_2Net and high-fidelity numerical simulation results for key variables at the forecasted time of 2520 days. The comparisons are made for two distinct permeability scenarios, labeled as Permeability #2 and Permeability #3, which are shown in Fig. 6. Notably, R_s and S_g are derived from z_{CO_2} and P_l. The mean relative errors for z_{CO_2} stand at 0.74% and 0.67% for the first and second test cases, respectively. For P_l, CO_2PCNet presents mean errors of 4.01% and 2.92%, suggesting high fidelity in its predictions. Conversely, CO_2Net, while offering reasonable approximations, tends toward larger errors, particularly with P_l predictions where the discrepancy markedly increases ($\delta_P = 13.91\%$ and 9.57%). Despite encountering some isolated high values due to the response discontinuity, mainly in R_s, which is an intrinsic characteristic observed in complex system, the CO_2PCNet model still maintains robust performance.
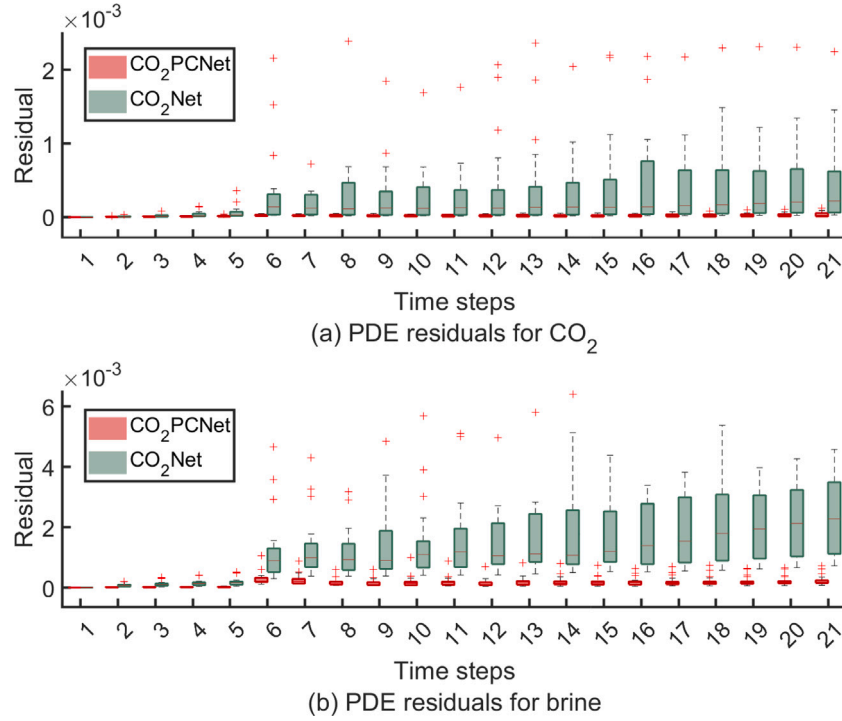
Fig. 13. Residual analysis for two components CO_2 and brine (Eq. (2.7)) for 20 random test cases.

Fig. 12 illustrates the mean relative error trends (Eqs. (4.3) and (4.4)) of CO_2PCNet and CO_2Net over a period of 2520 days. The figure presents evaluation metrics for two individual test cases and results across 200 test cases, providing a perspective on the accuracy of each model in predicting key variables of CO_2sequestration. In all test cases, CO_2Net can provide satisfactory short-term forecasts. However, CO_2PCNet consistently achieves lower mean relative errors for both CO_2 mole fraction (δ_z) and liquid pressure (δ_P) compared to CO_2Net, reflecting its excellent predictive accuracy.

A statistical comparison of residuals of PDEs, reflecting the mass conservation for CO_2 and brine over time as predicted by CO_2PCNet and CO_2Net across 20 random test cases is presented in Fig. 13. CO_2PCNet's performance is distinguished by a narrow range of residuals, with medians around 10^{-5} for both CO_2 and brine, demonstrating its consistent precision and adherence to conservation principles. Conversely, CO_2Net exhibits a wider residual distribution, with median values typically in the 10^{-4} range, suggesting a less precise agreements with mass conservation laws.

4.6. Performance comparisons

In this section, we evaluate CO_2PCNet's performance against the Auto-regressive Encoder–Decoder (AR-ED), a commonly utilized neural network framework in related studies (Zhang et al., 2023b). Although AR-ED shares a foundational architecture and physics constraints with CO_2PCNet, it does not incorporate the ConvLSTM component, a crucial element of CO_2PCNet that enriches its ability to process and predict temporal sequences within spatial contexts.

In Figs. 14 and 15, we evaluate the predictive performance of both models against reference values for a random test case at 2520 days, as well as their accumulate error evolution over a period of 2520 days. CO_2PCNet's predictions (in red) demonstrate a high degree of fidelity to the reference data, aligning closely with the ideal prediction line. This is quantitatively supported by a coefficient of determination (R^2) of 0.9944 for z_{CO_2} predictions. In contrast, AR-ED achieves an R^2 of 0.9793, signifying a slightly lower correlation with the simulation data.

Regarding P_l, AR-ED struggles to fully capture the dynamics of the full-cycle process, which is attributed to the model's limited capacity to capture the elliptic nature of pressure changes over injection and post-injection phases. This divergence demonstrates the critical role of ConvLSTM for capturing the complex subsurface CO_2 behavior over time.

5. Discussions and conclusions

In this work, we proposed the physics-constraint neural network (CO_2PCNet), a novel deep learning framework for CO_2 storage in deep saline aquifer. By honoring the physical constraints, CO_2PCNet provides robust predictions that are consistent with physics-based numerical simulations.

Through comprehensive evaluation, CO_2PCNet demonstrated excellent performance over baseline models such as CO_2Net and the Auto-regressive Encoder–Decoder (AR-ED), particularly in long-term forecasting. CO_2Net can offer reasonable estimates in the short term, however it falls short in longer period. Similarly, the AR-ED model is shown to be less capable when it comes to capturing the full dynamics of the system over longer periods, especially in regards to pressure predictions. Here, long-term refers to predictions extending six time steps beyond the training dataset, while short-term represents two or three time steps. In contrast, the integration of ConvLSTM layers in CO_2PCNet enhances its ability to capture the inherent spatial–temporal dependencies during the full-cycle process. Moreover, the incorporation of fundamental governing equations and boundary conditions ensures that the predictions remain consistent to the underlying physical laws.

This work successfully incorporates essential aspects of CO_2 storage in saline aquifers regarding the hydrodynamic trapping. Subsequent studies may apply CO_2PCNet to tackle challenges such as history matching and optimization of storage strategy, potentially incorporating more comprehensive geological and operational parameters to reflect the full complexity of CO_2 storage dynamics under varying conditions.
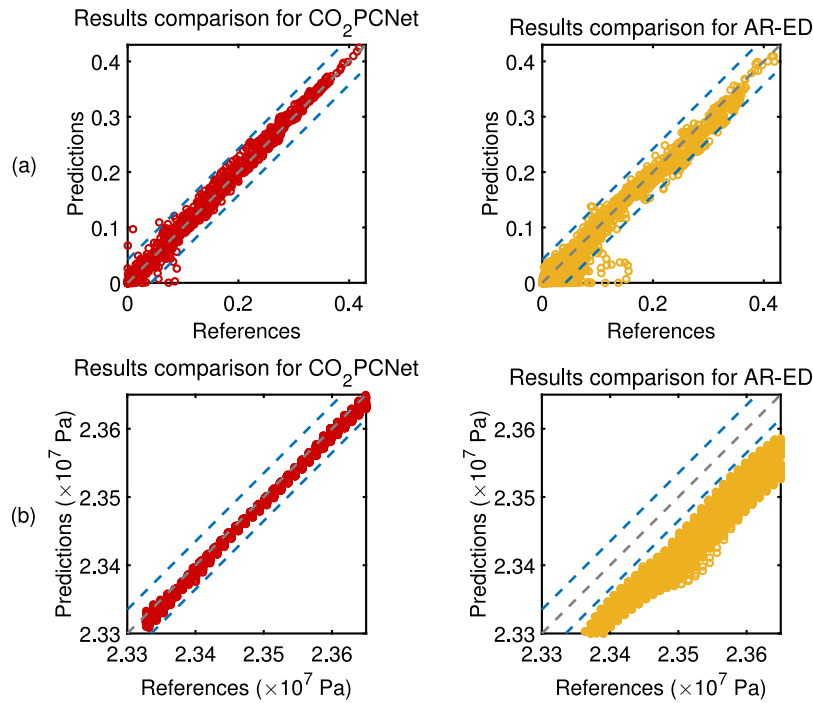
Fig. 14. Scatter Plots of Predictions vs. Reference Values at 2520 days: (a) z_{CO_2} and (b) P_l. CO_2PCNet predictions are shown in red (left), and AR-ED predictions in yellow (right). The dashed gray lines represent perfect predictions, and the blue dashed lines indicate a $\pm 10\%$ error range around the perfect predictions.
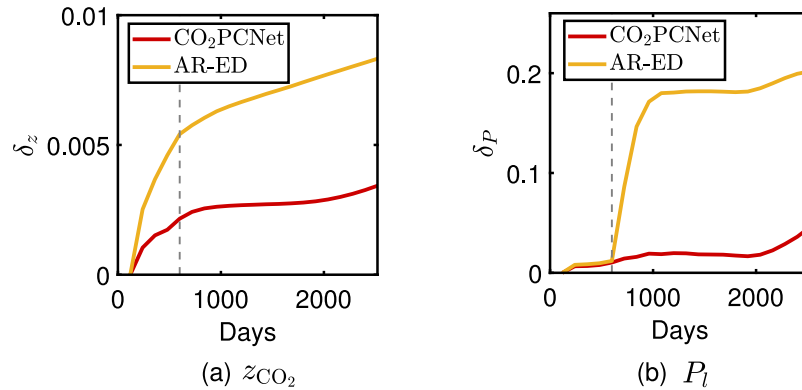

Fig. 15. Mean relative error trends for CO_2PCNet and AR-ED over a period of 2520 days in a test case. The vertical dashed lines represent the stop of CO_2 injection.

CRediT authorship contribution statement

Mengjie Zhao: Writing – original draft, Validation, Methodology, Conceptualization. **Yuhang Wang:** Writing – review & editing, Supervision, Software, Methodology, Conceptualization. **Marc Gerritsma:** Writing – review & editing, Supervision, Methodology, Conceptualization. **Hadi Hajibeygi:** Writing – review & editing, Software, Methodology, Funding acquisition, Conceptualization.

Declaration of competing interest

The authors declare that they have no known competing financial interests or personal relationships that could have appeared to influence the work reported in this paper.

Acknowledgments

Data availability

Data will be made available on request.

References

Celia, M.A., Bachu, S., Nordbotten, J.M., Bandilla, K.W., 2015. Status of CO_2 storage in deep saline aquifers with emphasis on modeling approaches and practical simulations. Water Resour. Res. 51 (9), 6846–6892.

Cusini, M., Fryer, B., van Kruijsdijk, C., Hajibeygi, H., 2018. Algebraic dynamic multilevel method for compositional flow in heterogeneous porous media. J. Comput. Phys. 354, 593–612.

Feng, Z., Tariq, Z., Shen, X., Yan, B., Tang, X., Zhang, F., 2024. An encoder-decoder ConvLSTM surrogate model for simulating geological CO_2 sequestration with dynamic well controls. Gas Science and Engineering 125, 205314.

Geneva, N., Zabaras, N., 2020. Modeling the dynamics of PDE systems with physics-constrained deep auto-regressive networks. J. Comput. Phys. 403, 109056.

Goodfellow, I., Bengio, Y., Courville, A., 2016. Deep Learning. MIT Press.

Goswami, S., Yin, M., Yu, Y., Karniadakis, G.E., 2022. A physics-informed variational DeepONet for predicting crack path in quasi-brittle materials. Comput. Methods Appl. Mech. Engrg. 391, 114587.

Hajibeygi, H., Tchelepi, H.A., 2014. Compositional multiscale finite-volume formulation. SPE J. 19 (02), 316–326.

Hochreiter, S., Schmidhuber, J., 1997. Long short-term memory. Neural Computation 9 (8), 1735–1780.

Ide, S.T., Jessen, K., Orr Jr., F.M., 2007. Storage of CO_2 in saline aquifers: Effects of gravity, viscous, and capillary forces on amount and timing of trapping. Int. J. Greenh. Gas Control 1 (4), 481–491.

Jiang, S., Durlofsky, L.J., 2024. History matching for geological carbon storage using data-space inversion with spatio-temporal data parameterization. Int. J. Greenh. Gas Control 134, 104124.

Ju, X., Hamon, F.P., Wen, G., Kanfar, R., Araya-Polo, M., Tchelepi, H.A., 2023. Learning CO_2 plume migration in faulted reservoirs with graph neural networks. arXiv preprint arXiv:2306.09648.

Karniadakis, G.E., Kevrekidis, I.G., Lu, L., Perdikaris, P., Wang, S., Yang, L., 2021. Physics-informed machine learning. Nat. Rev. Phys. 3 (6), 422–440.

Kingma, D.P., Ba, J., 2014. Adam: A method for stochastic optimization. arXiv preprint arXiv:1412.6980.

Krevor, S., De Coninck, H., Gasda, S.E., Ghaleigh, N.S., de Gooyert, V., Hajibeygi, H., et al., 2023. Subsurface carbon dioxide and hydrogen storage for a sustainable energy future. Nat. Rev. Earth Environ. 4 (2), 102–118.

Krizhevsky, A., Sutskever, I., Hinton, G.E., 2012. Imagenet classification with deep convolutional neural networks. Adv. Neural Inf. Process. Syst. 25.

LeCun, Y., Bengio, Y., Hinton, G., 2015. Deep learning. Nature 521 (7553), 436–444.

Liu, M., Grana, D., 2020. Petrophysical characterization of deep saline aquifers for CO_2 storage using ensemble smoother and deep convolutional autoencoder. Adv. Water Resour. 142, 103634.

Lyu, X., Voskov, D., Rossen, W.R., 2021. Numerical investigations of foam-assisted CO_2 storage in saline aquifers. Int. J. Greenh. Gas Control 108, 103314.

Metz, B., Davidson, O., De Coninck, H., Loos, M., Meyer, L., 2005. IPCC Special Report on Carbon Dioxide Capture and Storage. Cambridge University Press, Cambridge.

Miocic, J.M., Gilfillan, S.M., Roberts, J.J., Edlmann, K., McDermott, C.I., Haszeldine, R.S., 2016. Controls on CO_2 storage security in natural reservoirs and implications for CO_2 storage site selection. Int. J. Greenh. Gas Control 51, 118–125.

Mo, S., Zabaras, N., Shi, X., Wu, J., 2019a. Deep autoregressive neural networks for high-dimensional inverse problems in groundwater contaminant source identification. Water Resour. Res. 55 (5), 3856–3881.

Mo, S., Zhu, Y., Zabaras, N., Shi, X., Wu, J., 2019b. Deep convolutional encoder-decoder networks for uncertainty quantification of dynamic multiphase flow in heterogeneous media. Water Resour. Res. 55 (1), 703–728.

Nordbotten, J.M., Celia, M.A., 2006. Similarity solutions for fluid injection into confined aquifers. J. Fluid Mech. 561, 307–327.

Omosebi, O.A., Oldenburg, C.M., Reagan, M., 2022. Development of lean, efficient, and fast physics-framed deep-learning-based proxy models for subsurface carbon storage. Int. J. Greenh. Gas Control 114, 103562.

Orr Jr., F.M., 2018. Carbon capture, utilization, and storage: an update. SPE J. 23 (06), 2444–2455.

Pawar, R.J., Bromhal, G.S., Carey, J.W., Foxall, W., Korre, A., Ringrose, P.S., et al., 2015. Recent advances in risk assessment and risk management of geologic CO_2 storage. Int. J. Greenh. Gas Control 40, 292–311.

Raissi, M., Perdikaris, P., Karniadakis, G.E., 2019. Physics-informed neural networks: A deep learning framework for solving forward and inverse problems involving nonlinear partial differential equations. J. Comput. Phys. 378, 686–707.

Ramachandran, P., Zoph, B., Le, Q.V., 2017. Searching for activation functions. arXiv preprint arXiv:1710.05941.

Remy, N., Boucher, A., Wu, J., 2009. Applied Geostatistics with SGeMS: A User's Guide. Cambridge University Press.

Ren, P., Rao, C., Liu, Y., Wang, J.-X., Sun, H., 2022. PhyCRNet: Physics-informed convolutional-recurrent network for solving spatiotemporal PDEs. Comput. Methods Appl. Mech. Engrg. 389, 114399.

Ronneberger, O., Fischer, P., Brox, T., 2022. Convolutional networks for biomedical image segmentation. In: Medical Image Computing and Computer-Assisted Intervention–MICCAI 2015 Conference Proceedings.

Ruprecht, C., Pini, R., Falta, R., Benson, S., Murdoch, L., 2014. Hysteretic trapping and relative permeability of CO_2 in sandstone at reservoir conditions. Int. J. Greenh. Gas Control 27, 15–27.

Selma, L., Seigo, O., Dohle, S., Siegrist, M., 2014. Public perception of carbon capture and storage (CCS): A review. Renew. Sustain. Energy Rev. 38, 848–863.

Shi, X., Chen, Z., Wang, H., Yeung, D.-Y., Wong, W.-K., Woo, W.-c., 2015. Convolutional LSTM network: A machine learning approach for precipitation nowcasting. Adv. Neural Inf. Process. Syst. 28.

Sun, A.Y., 2020. Optimal carbon storage reservoir management through deep reinforcement learning. Appl. Energy 278, 115660.

Tang, M., Ju, X., Durlofsky, L.J., 2022. Deep-learning-based coupled flow-geomechanics surrogate model for CO_2 sequestration. Int. J. Greenh. Gas Control 118, 103692.

Tang, M., Liu, Y., Durlofsky, L.J., 2020. A deep-learning-based surrogate model for data assimilation in dynamic subsurface flow problems. J. Comput. Phys. 413, 109456.

Voskov, D.V., Tchelepi, H.A., 2012. Comparison of nonlinear formulations for two-phase multi-component EoS based simulation. J. Pet. Sci. Eng. 82, 101–111.

Wang, N., Chang, H., Zhang, D., 2021. Efficient uncertainty quantification and data assimilation via theory-guided convolutional neural network. SPE J. 26 (06), 4128–4156.

Wang, Y., Vuik, C., Hajibeygi, H., 2022. Analysis of hydrodynamic trapping interactions during full-cycle injection and migration of CO_2 in deep saline aquifers. Adv. Water Resour. 159, 104073.

Wang, Y., Zhang, Z., Vuik, C., Hajibeygi, H., 2024. Simulation of CO_2 storage using a parameterization method for essential trapping physics: FluidFlower benchmark study. Transp. Porous Media 151 (5), 1053–1070.

Wen, G., Hay, C., Benson, S.M., 2021a. CCSNet: a deep learning modeling suite for CO_2 storage. Adv. Water Resour. 155, 104009.

Wen, G., Tang, M., Benson, S.M., 2021b. Towards a predictor for CO_2 plume migration using deep neural networks. Int. J. Greenh. Gas Control 105, 103223.

Xu, F., Hajibeygi, H., Sluys, L.J., 2023. Adaptive multiscale extended finite element method (MS-XFEM) for the simulation of multiple fractures propagation in geological formations. J. Comput. Phys. 486, 112114.

Yan, B., Chen, B., Harp, D.R., Jia, W., Pawar, R.J., 2022. A robust deep learning workflow to predict multiphase flow behavior during geological CO_2 sequestration injection and post-injection periods. J. Hydrol. 607, 127542.

Zhang, Z., Wang, Y., Vuik, C., Hajibeygi, H., 2023a. An efficient simulation approach for long-term assessment of CO_2 storage in complex geological formations. In: SPE Reservoir Characterisation and Simulation Conference and Exhibition. OnePetro.

Zhang, Z., Yan, X., Liu, P., Zhang, K., Han, R., Wang, S., 2023b. A physics-informed convolutional neural network for the simulation and prediction of two-phase Darcy flows in heterogeneous porous media. J. Comput. Phys. 477, 111919.

Zhao, M., Wang, Y., Gerritsma, M., Hajibeygi, H., 2023. Efficient simulation of CO_2 migration dynamics in deep saline aquifers using a multi-task deep learning technique with consistency. Adv. Water Resour. 104494.

Zhao, M., Zhang, K., Chen, G., Zhao, X., Yao, J., Yao, C., et al., 2020. A classification-based surrogate-assisted multiobjective evolutionary algorithm for production optimization under geological uncertainty. SPE J. 25 (05), 2450–2469.

Zhu, Y., Zabaras, N., 2018. Bayesian deep convolutional encoder–decoder networks for surrogate modeling and uncertainty quantification. J. Comput. Phys. 366, 415–447.

Zhu, Y., Zabaras, N., Koutsourelakis, P.-S., Perdikaris, P., 2019. Physics-constrained deep learning for high-dimensional surrogate modeling and uncertainty quantification without labeled data. J. Comput. Phys. 394, 56–81.

Zoback, M.D., Gorelick, S.M., 2012. Earthquake triggering and large-scale geologic storage of carbon dioxide. Proc. Natl. Acad. Sci. 109 (26), 10164–10168.